From hydration repulsion to dry adhesion between asymmetric hydrophilic and hydrophobic surfaces

Matej Kanduč [*] [†] **and Roland R. Netz** [*]

[*]Department of Physics, Free University Berlin, D-14195 Berlin, Germany, and [†]Department of Theoretical Physics, J. Stefan Institute, SI-1000 Ljubljana, Slovenia

Submitted to Proceedings of the National Academy of Sciences of the United States of America

Utilizing all-atom molecular dynamics simulations at constant water chemical potential in combination with basic theoretical arguments, we study hydration-induced interactions between two overall charge-neutral yet polar planar surfaces with different wetting properties. Whether the water film between the two surfaces becomes unstable below a threshold separation and cavitation gives rise to long-range attraction, depends on the sum of the two individual surface contact angles. Consequently, cavitation-induced attraction also occurs for a mildly hydrophilic surface interacting with a very hydrophobic surface. If both surfaces are very hydrophilic, hydration repulsion dominates at small separations and direct attractive force contribution can – if strong enough – give rise to wet adhesion in this case. In between the regimes of cavitation-induced attraction and hydration repulsion we find a narrow range of contact angle combinations where the surfaces adhere at contact in the absence of cavitation. This dry adhesion regime is driven by direct surface–surface interactions. We derive simple laws for the cavitation transition as well as for the transition between hydration repulsion and dry adhesion, which favorably compare with simulation results in a generic adhesion state diagram as a function of the two surface contact angles.

Significance: Besides van-der-Waals and electrostatic interactions, surfaces in water experience solvation forces arising from the interfacial water structure and which become dominant at small surface separations. Using a combination of atomistic simulations and theoretical arguments, we construct the universal adhesion state diagram for two neutral surfaces with different water affinities. We find an intermediate regime of affinity combinations where the surfaces adhere to each other without an intervening water film. This dry adhesion also occurs for a surface with high water affinity if the other surface has a very low water affinity. These results not only explain how surfaces interact in water but are also relevant for designing synthetic surfaces that efficiently bind to particles with given surface properties.

According to the classical Derjaguin–Landau–Verwey–Overbeek (DLVO) theory, the interaction between hydrated surfaces is given by the sum of van-der-Waals (vdW) and screened electrostatic interactions [1]. Although this approach works well in many situations, sub-nanometer resolved force measurements between individual surfaces demonstrated that additional water-mediated interactions are dominant at small separations and depend crucially on the polarity or wetting properties of the surfaces [2–4]. Understanding these solvation-induced interactions is still a central issue in all fields concerned with forces between surfaces, colloids, and macromolecular aggregates in water.

As is well-known, the water film between two hydrophobic surfaces, characterized by water contact angles $\theta > 90^\circ$, becomes free-energetically unstable below a critical distance and cavitation leads in equilibrium to vapor bubble-induced long-ranged attraction [5–7]. Conversely, polar and overall neutral surfaces, characterized by small or vanishing contact angles, exhibit pronounced short-ranged repulsive forces, which decay exponentially with a characteristic length in the sub-nanometer range [8–11]. These so-called hydration forces arise from the complex interplay of surface group configurational degrees of freedom, desorption of hydration water from polar surface groups, and ordering of the inter-surface water film [4]. The understanding of hydration forces has recently been advanced by computer simulations that include explicit water molecules [12–14].

In the absence of direct surface–surface interactions, the transition between cavitation-induced attraction and hydration repulsion should coincide with the contact angle characterizing the border between hydrophilic and hydrophobic surface properties, i.e. $\theta = 90^\circ$. In contrast, experiments probing the interactions between similar neutral surfaces with well defined contact angles demonstrated that even hydrophilic surfaces exhibit short range attractions not accountable by vdW forces down to typical adhesive contact angles of $\theta_{\mathrm{adh}} = 65^\circ$–$80^\circ$ [15–18]. Comparable results were recently obtained in simulations, where the adhesion behavior was shown to depend crucially on the surface adhesion energy [19]. A transition between dry adhesion and hydration repulsion was seen for typical surface contact angle values in the range of $\theta_{\mathrm{adh}} = 65^\circ$–$85^\circ$, depending on the mechanical stiffness and the hydrogen-bonding capability of the surfaces [19], the values of θ_{adh} being quite similar to experiments [15–18].

The above mentioned references all deal with situations where the two interacting surfaces are identical in chemical surface structure and thus have the same contact angles. Although of conceptual importance, this symmetric scenario constitutes an exception rather than a rule. Most practical situations involve two dissimilar surfaces, for example nano particles interacting with cell membranes [20] or weak protein–protein interactions [21]. In fact, a number of experimental model studies addressed the interactions between dissimilar surfaces and the particularly interesting case of hydrophobic–hydrophilic surfaces [2,3,22–26]. The results are rather multifaceted and can not be easily cast in a unified picture, yet, in one study an empirical sum rule for the interaction strength between two dissimilar surfaces in terms of the two surface contact angles was established [22].

To address these experimental systems, we investigate hydration-induced interaction by a combination of large scale molecular dynamics simulations and theoretical arguments. We study the interaction between two atomistically resolved self-assembled monolayers (SAMs) with different wetting properties in the presence of explicit water. Our primary goal is to unravel the underlying principles of hydration-induced interactions in the complete parameter space encompassing

Reserved for Publication Footnotes

all combinations from completely unpolar (hydrophobic) to extremely polar (hydrophilic) surfaces. In our simulation model, the surfaces contain polar groups and thus allow for inter-surface and water–surface hydrogen bonding, yet they are overall charge neutral to avoid additional complications due to double-layer interactions. We also derive laws for the cavitation transition and for the dry adhesion transition as a function of the two surface contact angles. As our main result, we present a two-dimensional adhesion diagram in terms of the contact angles of the two surfaces in which we favorably compare the theoretical predictions for the cavitation and dry adhesion transitions with our explicit simulation results.

The cavitation transition signals the instability of the water layer below a critical surface separation. By a simple, yet exact derivation, we show that it depends on the sum of the two contact angles. It follows that cavitation can occur also on a hydrophilic surface if the other other confining surface is sufficiently hydrophobic, which is a surprising result with a number of practical consequences. The cavitation transition is universal in the sense that it does not depend on any other system property besides the two surface contact angles. It is important to keep in mind that the cavitation kinetics is characterized by a high nucleation barrier, consequently the water layer might experimentally remain metastable for extended times even for surface separations much smaller than the predicted cavitation threshold [27, 28]. Once cavitation has occurred, the two surfaces are pushed together by the ambient pressure, by direct surface–surface interactions, and for curved surfaces by attractive force components that arise from bubble deformation energetics, which have been amply discussed before [29]. We note that we use a slightly modified terminology that is adjusted to the present general discussion involving two different surfaces: We do not refer to the attraction induced by cavitation as *hydrophobic attraction*, as is commonly done in literature, reflecting the fact that this type of attraction also occurs between a pair of hydrophobic and hydrophilic surfaces if the sum of the contact angles is larger than 180°.

The dry adhesion transition denotes the threshold between the situation where hydration repulsion prevents direct surface–surface contact and the situation where direct surface–surface interactions induce dry adhesion. This transition occurs at contact angles smaller than the cavitation transition, i.e. in a region of surface parameters where the water film between the surfaces is stable at large separations. In other words, we predict a regime of dry adhesion for intermediate surface contact angles, which is not caused or accompanied by cavitation. The extent of the dry adhesion regime depends on the magnitude of direct interactions between the surfaces and thus cannot be predicted based on single surface properties (i.e., the contact angles) alone. Using a perturbative expansion scheme, we derive an asymptotic expression for the transition between dry adhesion and hydration repulsion in terms of the non-polar and polar surface–surface interaction strengths, which agrees very well with the explicit simulation results for not too asymmetric surfaces.

Results

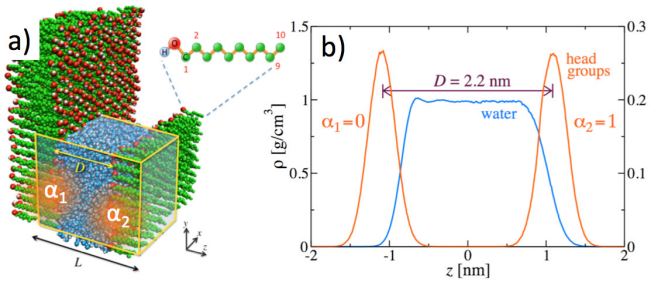

Fig. 1. (a) Snapshot of the periodic simulation system: Two parallel surfaces consisting of hydroxyl-terminated alkane chains with different polarity parameters α_1 and α_2 interact across a water layer at fixed chemical potential. (b) Density profiles of water and head-group oxygens for the asymmetric scenario $\alpha_1 = 0$ and $\alpha_2 = 1$.

Our atomistic model for the interacting surfaces consists of two layers, each of 100 anchored alkane chains with terminal hydroxyl (-OH) head groups separated by a water layer and placed in a periodic box, see Fig. 1a for a simulation snapshot. The surface polarity is controlled by scaling the hydroxyl partial charges by parameters α_1 and α_2 in the range [0, 1], respectively. The values $\alpha_{1,2} = 1$ correspond to the completely polar and $\alpha_{1,2} = 0$ to the completely unpolar cases. We span the complete $\alpha_{1,2}$ parameter space by explicitly simulating a total of 66 different polarity combinations, from which a global adhesion diagram is then constructed by interpolation. The chains are arranged on a hexagonal lattice with an area per chain of $0.234\,\mathrm{nm}^2$, stabilized by weak harmonic restraining potentials. As a result, the surfaces are rather soft, meaning that water layering effects are weak and the water density profiles exhibit only small structural oscillations, as shown in Fig. 1b. As it turns out crucial for our analysis, using novel simulation technologies, the water chemical potential μ_0 is kept fixed at the bulk value with a precision of $\pm 0.01\,k_\mathrm{B}T$ [14] and surface contact angles are obtained with a precision of $\pm 1°$ [19]. This allows to obtain the normal interaction surface pressure in the experimentally relevant ensemble of a fixed and prescribed chemical potential. For further simulation details see *SI Appendix*.

Water adsorption on a single surface. We first focus on a single surface. In practice, we simulate two surfaces at a large enough surface–surface distance of $D = 4\,\mathrm{nm}$ so that they do not interfere. This is an important preliminary step, since we find stable water wetting films in the asymmetric case of a hydrophilic surface interacting with a hydrophobic surface [30, 31]. The wetting coefficient k_w measures the surface affinity for water and is defined as

$$k_\mathrm{w} = (\gamma_\mathrm{sv} - \gamma_\mathrm{sw})/\gamma, \qquad [1]$$

where γ_sv, γ_sw, γ correspond to the surface–vapor, surface–water, and water–vapor interfacial free energies. It is related to the surface contact angle θ via Young's equation $k_\mathrm{w} = \cos\theta$ and in our simulations determined via a modified thermodynamic integration method [19], as explained in detail in *SI Appendix*. Fig. 2 shows k_w (black circles) at fixed excess water chemical potential $\mu_0^\mathrm{ex} = -29.03\,\mathrm{kJ/mol}$ corresponding to bulk water at $T = 300\,\mathrm{K}$ and pressure $p_0 = 1\,\mathrm{bar}$ [32]. The wetting coefficient k_w grows with the polarity parameter α. In the completely unpolar case, for $\alpha = 0$, we find $k_\mathrm{w} = -0.7$, corresponding to a contact angle of $\theta = 135°$. The threshold

between hydrophobic, $\theta > 90^\circ$, and hydrophilic, $\theta < 90^\circ$, surface behavior is crossed for $\alpha = 0.62$. At $\alpha \simeq 0.9$ we observe a wetting transition, i.e. for $\alpha < 0.9$ the surface is partially wet and characterized by a non-zero finite contact angle, while for $\alpha > 0.9$ the surface is completely wetted by a macroscopic water film and $k_w = 1$ (equivalent to $\theta = 0^\circ$). We also show the vacuum wetting coefficient in the absence of water adsorption, $k_w^{vac} = (\gamma_{s,vac} - \gamma_{sw})/\gamma$ (red circles), which is determined from the surface–vacuum interfacial energy $\gamma_{s,vac}$ and which is strictly larger than the true wetting coefficient k_w. The reduction of the wetting coefficient from k_w^{vac} to k_w is caused by the formation of a water adsorption film. The film areal number density n_A in the inset (blue squares) grows towards the wetting transition at $\alpha \simeq 0.9$ [31, 33]. Interestingly, the water film reaches a mean thickness of about 0.1 nm (converted from an areal density of $n_A \sim 3\,\mathrm{nm}^{-2}$ assuming bulk water density in the film), corresponding roughly to a single layer of water molecules, only very close to the wetting transition at a contact angle of roughly $\theta \simeq 30^\circ$ (see *SI Appendix* for snapshots of water films). Although water adsorption is thus weak as judged by the adsorbed amount, it sensitively modifies the equilibrium contact angle, and therefore has to be properly taken into account. This follows from the pronounced difference between the vacuum wetting coefficient (red line) and the equilibrium wetting coefficient (black line), which accounts for the wetting film formation.

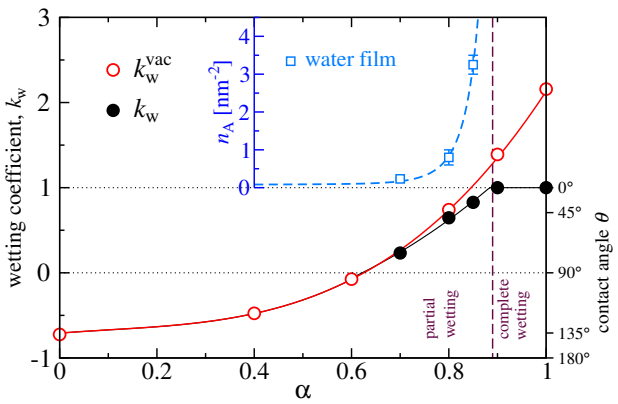

Fig. 2. Single surface results: Wetting coefficient k_w as a function of the surface polarity parameter α (black circles), the corresponding contact angle θ is shown on the right axis. The wetting transition, defined by $\theta = 0^\circ$, occurs at $\alpha \simeq 0.9$. Red circles denote the vacuum wetting coefficient k_w^{vac} obtained in the absence of a water film at the surface–vapor interface. The areal water density of the adsorbed water film n_A is shown in the inset. Lines are guides to the eye.

Interactions between two surfaces: Simulation results. Using the thermodynamic extrapolation method [19], we determine the normal interaction pressure between two surfaces in the presence of water at a fixed chemical potential corresponding to bulk water. Using this method, as we change the distance between the plates, the number of water molecules is always adjusted to satisfy the hydration equilibrium. By integrating the pressure–distance curves, we obtain the hydrated free energy $f(D)$ as a function of distance D. We define D as the mean distance between the oxygen head groups on the two opposing surfaces. In Fig. 3 we show $f(D)$ in the hydrated state (blue lines) for three exemplary polarity combinations that illustrate the regimes of a) hydration repulsion, b) dry adhesion without cavitation, and c) cavitation-induced attraction (corresponding pressure curves are presented in *SI Appendix*). In all three examples the first surface is completely unpolar ($\alpha_1 = 0$) and characterized by a contact angle $\theta_1 = 135^\circ$, corresponding to a very hydrophobic surface. Note that we define $f(D = \infty) = 0$, so all free energies are expressed with respect to the reference state corresponding to hydrated surfaces at large separations of about $D \simeq 1.5$ nm.

In Fig. 3a the second surface is characterized by a rather high polarity factor of $\alpha_2 = 0.9$, right at the wetting transition, corresponding to a contact angle of $\theta_2 = 0^\circ$ (compare Fig. 2). The hydrated free energy exhibits a very weak attractive minimum at a separation around $D \simeq 0.8$ nm, for smaller separations we observe strong hydration repulsion. The green horizontal dashed line indicates the free energy of the cavitated state at separations where the surfaces do not interact with each other (i.e., $D > 1.2$ nm), $f_{cav}^{\infty} = \gamma_{s1v} - \gamma_{s1w} + \gamma_{s2v} - \gamma_{s2w} + p_0 D$, which includes the effect of the formation of a thin water film on the polar surface. One sees that f_{cav}^{∞} lies above the $f(D)$ curve, reflecting that for this surface polarity combination, the hydrated state is stable against cavitation. This is a quite surprising result as it shows that even a very hydrophobic surface with a contact angle of $\theta_1 = 135^\circ$ is fully hydrated if the second surface is very polar. Further below we will demonstrate that this simulation finding is in full accordance with our theoretical analysis of the cavitation transition between asymmetric surfaces. For comparison, we also compute the free energy $f_{vac}(D)$ for two surfaces interacting in the absence of water, i.e. when the water slab is replaced by vacuum (red line). This curve even lies above the cavitated state free energy f_{cav}^{∞} (green horizontal line), showing that water film formation on the polar surface lowers the free energy significantly. At very small separations, when the water content (shown by the turquoise line in Fig. 3a) tends to zero, the $f(D)$ and $f_{vac}(D)$ curves continuously merge. In the *SI Appendix* we demonstrate that the free energy minimum of the hydrated state at $D \simeq 0.8$ nm, which corresponds to wet adhesion, is caused by a combination of vdW and more complex water-mediated interactions between the surfaces. Because of the strong hydration repulsion at smaller separation, we term this scenario the hydration repulsion regime.

At a slightly smaller polarity of the second surface, $\alpha_2 = 0.83$, leading to a contact angle of $\theta_2 = 36^\circ$, while still $\theta_1 = 135^\circ$, we see in Fig. 3b that for surface separations larger than a nanometer f_{cav}^{∞} and $f_{vac}(D)$ still are above the hydrated free energy $f(D)$, meaning that the hydrated state is stable against cavitation at large D. However, the water layer becomes unstable with respect to dry adhesion at surface contact. In other words, for this contact angle combination the absolute free energy minimum is furnished by the vacuum state at the adhesive separation D_{adh}. The surfaces adhere stably to each other in the absence of water because of direct surface–surface interactions. This occurs without a cavitation instability at large separations, we name this scenario the *dry adhesion regime*.

At even smaller polarity $\alpha_2 = 0.7$ of the second surface in Fig. 3c, corresponding to a contact angle of $\theta_2 = 75^\circ$, the cavitated state (green dashed line) is preferred over the hydrated state (blue line) already at large surface separations. In equilibrium, the surfaces are therefore predicted to experience long-range cavitation-induced attraction. Note that in our simulations the hydrated state stays metastable down to small surface separations of about $D \simeq 1$ nm. For smaller separations we cannot generate stable water films because of pronounced density fluctuations leading to spontaneous cavitation effects (similar to experimental findings [28]).

In the following, we will derive theoretical laws for the transitions between the regimes of cavitation-induced attraction, dry adhesion without cavitation, and hydration repulsion

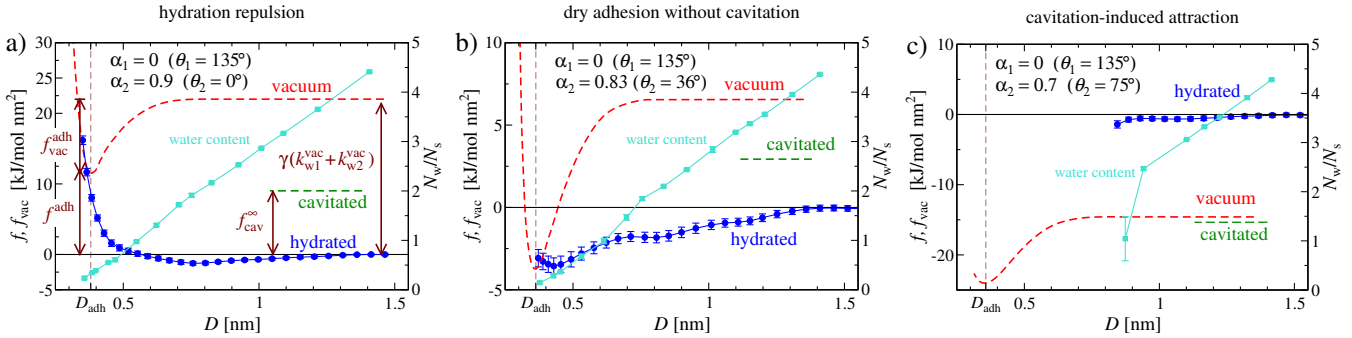

Fig. 3. Simulation results for the surface free energy in the hydrated state, $f(D)$ (dark blue lines), and in the vacuum state, $f_{\rm vac}(D)$ (red dashed lines), for three surface polarity combinations that illustrate the scenarios of (a) hydration repulsion, (b) dry adhesion without cavitation, and (c) cavitation-induced attraction. The number of water molecules per surface group $N_{\rm w}/N_{\rm s}$ is shown in turquoise (right scale). The green horizontal dashed lines denote the cavitation free energy at infinite separation $f_{\rm cav}^{\infty}$, which includes the effects of formation of water wetting films on the surfaces.

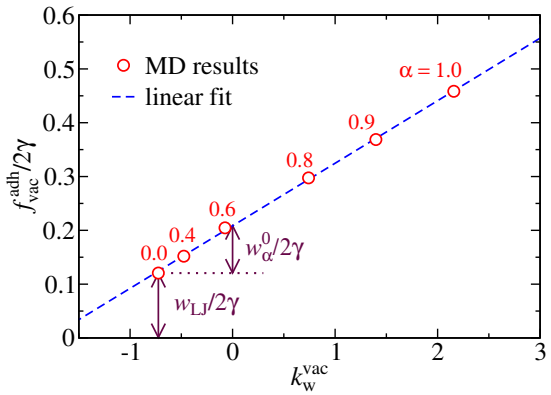

Fig. 4. Adhesion free energy in vacuum $f_{\rm vac}^{\rm adh}$ as a function of the vacuum wetting coefficient $k_{\rm w}^{\rm vac}$ for the symmetric scenario, $\alpha_1 = \alpha_2 \equiv \alpha$.

and thereby place the exemplary simulation results shown in Fig. 3 in a global state diagram.

Cavitation transition between dissimilar surfaces. The free energy of the cavitated state with respect to the hydrated state is $f_{\rm cav}^{\infty} = \gamma_{\rm s1v} - \gamma_{\rm s1w} + \gamma_{\rm s2v} - \gamma_{\rm s2w} + p_0 D$ and consists of the interface free energy differences and the work needed to expel the water slab into the reservoir at bulk pressure p_0. The pressure contribution can for the nanometer scale separations D considered in this paper be neglected (corrections due to finite pressure and finite surface areas are discussed in *SI Appendix*). Using the definitions of the wetting coefficients $k_{\rm w1} = \cos\theta_1 = (\gamma_{\rm s1v} - \gamma_{\rm s1w})/\gamma$ and $k_{\rm w2} = \cos\theta_2 = (\gamma_{\rm s2v} - \gamma_{\rm s2w})/\gamma$, the cavitation condition $f_{\rm cav}^{\infty} = 0$ can be rewritten as $k_{\rm w1} + k_{\rm w2} = \cos\theta_1 + \cos\theta_2 = 0$ or, equivalently (see *SI Appendix*),

$$\theta_1 + \theta_2 = 180^\circ. \qquad [2]$$

In the symmetric case of equal contact angles $\theta_1 = \theta_2 \equiv \theta$ one recovers the standard cavitation threshold of $\theta = 90^\circ$. For the general asymmetric case the cavitation law in Eq. (2) predicts that cavitation can occur even on a hydrophilic surface if the other surface is sufficiently hydrophobic. On the other hand, cavitation on a very hydrophobic surface is prevented if the other surface is sufficiently hydrophilic, in full accord with our simulation results shown in Fig. 3a. Note that Eq. (2) has previously been discussed in connection with experimental results [24].

Dry adhesion transition between dissimilar surfaces. We now derive the asymptotic law describing the transition between the hydration repulsion and the dry adhesion regimes. In the former regime the adhesive free energy at contact $f^{\rm adh} \equiv f_{\rm vac}(D_{\rm adh})$ is positive and therefore the equilibrium state involves a finite water slab thickness, as shown in Fig. 3a. In the dry adhesion regime, shown in Fig. 3b, the adhesive energy $f^{\rm adh}$ is negative while the water layer is stable against cavitation at larger separations. We define the dry adhesion transition by the condition $f^{\rm adh} = 0$. This definition neglects the presence of a wet adhesion state at finite water slab thickness, which only leads to negligible effects in our final adhesion phase diagram, but allows the derivation of a closed-form prediction for the adhesion transition. As graphically demonstrated in Fig. 3a by the vertical brown arrows, the adhesion free energy $f^{\rm adh}$ can be conveniently split into the vacuum free energy at large separations and the vacuum adhesion work,

$$f^{\rm adh} = \gamma(k_{\rm w1}^{\rm vac} + k_{\rm w2}^{\rm vac}) - f_{\rm vac}^{\rm adh}. \qquad [3]$$

We furthermore decompose the vacuum adhesion work as $f_{\rm vac}^{\rm adh} = w_{\rm LJ} + w_\alpha$ into the Lennard-Jones (LJ) component $w_{\rm LJ}$ and the polar component w_α. The term $w_{\rm LJ}$ represents the vdW interactions in the system and is in the simulations generated by LJ interactions between the SAM atoms. The term w_α is due to surface partial charges and reflects hydrogen bonding between surface groups, it only arises when both surfaces are polar. As shown in Fig. 4 for the symmetric case, $k_{\rm w1}^{\rm vac} = k_{\rm w2}^{\rm vac} \equiv k_{\rm w}^{\rm vac}$, the vacuum adhesion energy $f_{\rm vac}^{\rm adh}$ scales perfectly linearly with the vacuum wetting coefficient $k_{\rm w}^{\rm vac}$, we can thus write

$$f_{\rm vac}^{\rm adh} = w_{\rm LJ} + w_\alpha^0 + 2c\gamma k_{\rm w}^{\rm vac}. \qquad [4]$$

Here, $w_{\rm LJ} = 8.0\,{\rm kJ/mol\,nm^2}$, $w_\alpha^0 = 5.8\,{\rm kJ/mol\,nm^2}$, and $c = 0.115$ are determined by a linear fit and the condition that $w_\alpha = 0$ for vanishing polarity parameter $\alpha = 0$. In fact, the vacuum adhesion work between two identical surfaces is via this empirical relation shown to be linearly proportional to the surface water binding ability: As quantified by the coefficient c, the stronger a surface binds water, expressed via the vacuum wetting coefficient $k_{\rm w}^{\rm vac} = (\gamma_{\rm s,vac} - \gamma_{\rm sw})/\gamma$, the stronger it binds to a second surface of the same kind. For an asymmetric pair of surfaces, we expect a geometric combination rule for the polar contribution according to

$$w_\alpha(k_{\rm w1}^{\rm vac}, k_{\rm w2}^{\rm vac}) = \sqrt{w_\alpha(k_{\rm w1}^{\rm vac}, k_{\rm w1}^{\rm vac}) w_\alpha(k_{\rm w2}^{\rm vac}, k_{\rm w2}^{\rm vac})}, \qquad [5]$$

since the dipolar interaction between two surfaces in vacuum is proportional to the product of the partial charges on the

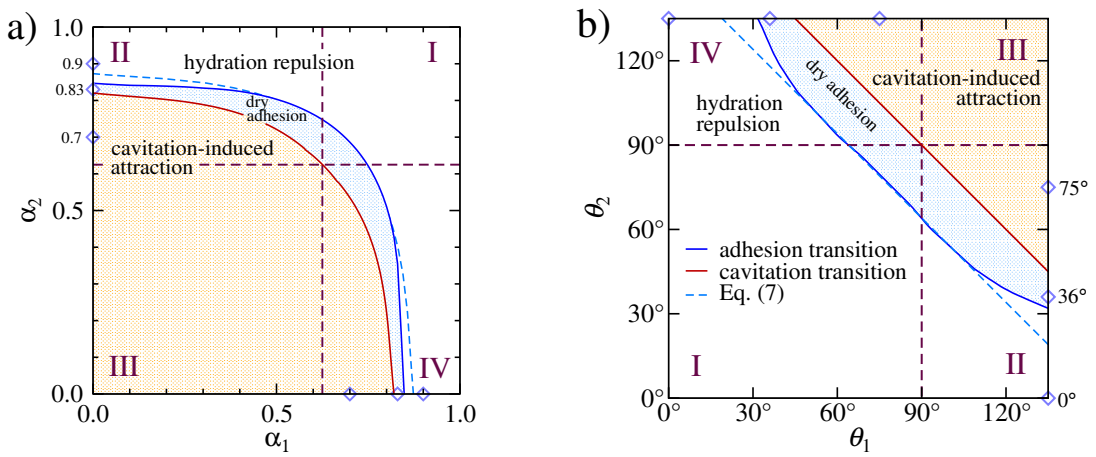

Fig. 5. Adhesion diagram for two surfaces represented in terms of (a) the two surface polarity parameters α_1 and α_2 and (b) the two surface contact angles θ_1 and θ_2, featuring the regimes of hydration repulsion (white), dry adhesion without cavitation (blue), and cavitation-induced attraction (orange). The asymptotic law for the adhesion transition, Eq. 7 (blue dashed line) agrees well with the simulation results (solid blue line) for not too asymmetric surfaces. The cavitation transition that separates the dry adhesion and the cavitation-induced attraction regimes is exactly described by the law Eq. 2 (red solid line). The diamonds indicate the three scenarios considered in Fig. 3.

two surfaces. This combination rule was earlier established based on experimental data [22] and is validated in *SI Appendix* using our simulation results. Combining Eqs. (3–5), we obtain the following conditional equation for the adhesion transition, determined by $f^{\rm adh} = 0$,

$$\gamma(k_{\rm w1}^{\rm vac} + k_{\rm w2}^{\rm vac}) = w_{\rm LJ} + \sqrt{(w_\alpha^0 + 2c\gamma k_{\rm w1}^{\rm vac})(w_\alpha^0 + 2c\gamma k_{\rm w2}^{\rm vac})}. \quad [6]$$

For small wetting coefficients $k_{\rm w1}^{\rm vac}$ and $k_{\rm w2}^{\rm vac}$ we can expand the square root and finally obtain for the adhesion transition (see *SI Appendix* for details)

$$\theta_1 + \theta_2 \simeq 2\theta_{\rm adh}. \quad [7]$$

Here, the adhesive contact angle $\theta_{\rm adh}$ depends on the previously determined surface interaction parameters as

$$\cos\theta_{\rm adh} = (w_{\rm LJ} + w_\alpha^0)/[2\gamma(1-c)]. \quad [8]$$

As would be expected, the larger the LJ and the polar interaction energies $w_{\rm LJ}$ and w_α^0, the smaller the $\theta_{\rm adh}$, while a particularly decisive role is played by the coefficient c. In general, the vacuum adhesion work $w_{\rm LJ} + w_\alpha^0$ is positive, according to Eq. (4) this means that finite work is required to separate two surfaces characterized by $k_{\rm w}^{\rm vac} = 0$ or $\theta \approx 90°$. In that case, we see from Eq. (8) that $\cos\theta_{\rm adh} > 0$ or $\theta_{\rm adh} < 90°$, since $c < 1$. By comparison with Eq. (2) we thus conclude that the regime of dry adhesion without cavitation exists within a finite range of surface contact angles. For the model system studied in our case we find $\theta_{\rm adh} = 77°$, but it transpires from our analysis that $\theta_{\rm adh}$ can be much smaller and that the hydration repulsion regime can completely disappear.

Global adhesion state diagram. We present the resulting adhesion diagram in Fig. 5(a) in terms of the surface polarity parameters α_1 and α_2, and in Fig. 5(b) in terms of the contact angles θ_1 and θ_2. The diagram is based on explicit simulations of 66 different surface polarity combinations and separates into three regimes, corresponding to hydration repulsion (for large polarity parameters or small contact angles), cavitation-induced attraction (for small polarity parameters or large contact angles), and within a thin strip between the latter two regimes, dry adhesion without cavitation.

Experimentally most relevant is the diagram in terms of the two contact angles in Fig. 5(b). Owing to the fact that both cavitation and adhesion transitions depend on the sum $\theta_1 + \theta_2$, see Eqs. (2) and (7), the adhesion diagram has a simple but crucial topological structure: For any path going from the hydration repulsion regime to the cavitation regime, one crosses the dry adhesion regime without cavitation. The width of this intermediate regime depends on the adhesive contact angle $\theta_{\rm adh}$, which in the present simulation model employing hydroxyl surface groups is given by $\theta_{\rm adh} = 77°$. It has been shown to vary between $\theta_{\rm adh} = 67°$ and $\theta_{\rm adh} = 83°$ for different surface structures in our previous work concerned with symmetric surfaces [19]. Clearly, the smaller the $\theta_{\rm adh}$, the larger the dry adhesion regime. While the blue solid line shows the dry adhesion transition directly determined from the simulations, the asymptotic law Eq. (7) is shown by a blue dashed line and indeed seen to be valid except for very asymmetric surface combinations. The cavitation law, described by Eq. (2), is shown by a red line and does not rely on any approximation, consequently, our simulation data are in full agreement. Probably the most surprising feature of the adhesion state diagram in Fig. 5(b) is that the dry adhesion regime extends into the off-diagonal corners, corresponding to asymmetric hydrophilic–hydrophobic surface combinations. We see that there exists an extended range of contact angle combinations where a hydrophilic surface with $\theta_1 < 90°$ adheres to a second surface in a dry state, in particular if that second surface is sufficiently hydrophobic. Conversely, a hydrophobic surface with $\theta_1 > 90°$ can be prevented from exhibiting cavitation and even from adhering to a second surface in a dry fashion if the second surface is sufficiently hydrophilic. Our adhesion diagram thus presents definite rules for controlling surface adhesion properties in terms of the surface contact angles (in other words, in terms of the interfacial free energies).

Discussion

Utilizing an atomistic model for the interaction between two hydroxylated surfaces with different polarities in the presence of explicit water, in conjunction with simulation methods that allow to account for the constant water chemical potential and to determine accurate surface contact angles, we establish a general adhesion diagram with three regimes: Hydration repulsion for very polar surfaces, cavitation for unpolar surfaces, and, in between, dry adhesion without cavitation. Our derived

laws for the cavitation transition and the dry adhesion transition both depend on the sum of the contact angles of the two surfaces, in good agreement with explicit simulation results for not too asymmetric surfaces. This means that the regime of dry adhesion without cavitation in the adhesion state diagram spanned by the two surface contact angles forms a strip between the hydration repulsion and cavitation regimes, in good agreement with a host of experimental findings for different systems [2, 3, 22–26]. Our theoretical analysis shows that this dry adhesion regime necessarily exists and that it becomes more pronounced the stronger the direct surface–surface interactions are. One important conclusion is that for a wide range of polar surfaces it should therefore be possible to design a counter-surface that will bind to that surface in a very tight dry-adhesion complex if the surface contact angles fall into the dry adhesion regime defined by the laws given in Eqs. (2) and (7).

Note that our simulations in the hydration repulsion regime yield a wet adhesion state at a finite water slab thickness. Clearly, explicit-water simulations are not well suited to study details of this wet adhesion state, since the vdW surface forces are rather small and in simulations difficult to be estimated reliably. As an additional complication, finite LJ cutoffs are employed in MD simulation force-fields and give rise to cutoff artifacts at large surface separations (see *SI Appendix* for more details). Obviously, simulations will have to be combined with continuum modeling to make progress in understanding wet adhesion properties [34].

The adhesion contact angle for our explicit simulation model, based on hydroxyl surface groups whose partial charges are continuously varied, is given by $\theta_{\rm adh} = 77^\circ$, leading to a rather narrow strip of dry adhesion in the diagram in Fig. 5b. In future simulations different experimentally relevant surface groups will be studied. One particularly important question is to understand how to control the adhesion angle $\theta_{\rm adh}$, which is via Eq. (8) linked to the sum of the non-polar (LJ) and polar surface–surface interactions. In *SI Appendix* we demonstrate that the adhesion transition is on the microscopic level determined by the balance of surface–surface and surface–water hydrogen bonds. This suggests that cleverly designed surfaces with donor–acceptor hydrogen-bonding pairs presumably decrease $\theta_{\rm adh}$ considerably. A further question to be tackled in the future is, how the presence of surface charges modifies the solvation interaction and in particular the short-range adhesion behavior.

Acknowledgments. We acknowledge funding from the DFG via SFB 765.

1. Israelachvili J, Intermolecular and Surface Forces. London: Academic, 1992.
2. Christenson HK and Claesson PM (2001) Direct measurements of the force between hydrophobic surfaces in water. Adv. Coll. Int. Sci., 91, no. 3, pp. 391–436.
3. Meyer EE, Rosenberg KJ, and Israelachvili J (2006)Recent progress in understanding hydrophobic interactions. Proc. Natl. Acad. Sci., vol. 103, no. 43, pp. 15739–15746.
4. Parsegian VA and Zemb T (2011) Hydration forces: Observations, explanations, expectations, questions Curr. Opin. Colloid Interface Sci., vol. 16, pp. 618–624.
5. Christenson HK and Claesson PM (1988) Cavitation and the interaction between macroscopic hydrophobic surfaces. Science, vol. 239, no. 4838, pp. 390–392.
6. Lum K, Chandler D, and Weeks JD (1999)Hydrophobicity at small and large length scales. J. Phys. Chem. B, vol. 103, no. 22, pp. 4570–4577.
7. Huang X, Margulis CJ, and Berne BJ (2003) Dewetting-induced collapse of hydrophobic particles. Proc. Natl. Acad. Sci., vol. 100, no. 21, pp. 11953–11958.
8. Parsegian VA, Fuller N, and Rand R (1979) Measured work of deformation and repulsion of lecithin bilayers. Proc. Natl. Acad. Sci., vol. 76, no. 6, pp. 2750–2754.
9. Rand R and Parsegian VA, "Hydration forces between phospholipid bilayers," Biochimica et biophysica acta, vol. 988, no. 3, pp. 351–376, 1989.
10. Israelachvili JN and Pashley RM (1983) Molecular layering of water at surfaces and origin of repulsive hydration forces. Nature, vol. 306, pp. 249–250.
11. Marra J and Israelachvili J (1985) Direct measurements of forces between phosphatidylcholine and phosphatidylethanolamine bilayers in aqueous electrolyte solutions. Biochemistry, vol. 24, pp. 4608–4618.
12. Pertsin A, Platonov D, and Grunze M (2007) Origin of short-range repulsion between hydrated phospholipid bilayers: A computer simulation study. Langmuir, vol. 23, pp. 1388–1393.
13. Eun C and Berkowitz ML (2009) Origin of the hydration force: Water-mediated interaction between two hydrophilic plates. J. Phys. Chem. B, vol. 113, pp. 13222–13228.
14. Schneck E, Sedlmeier F, and Netz RR (2012) Hydration repulsion between biomembranes results from an interplay of dehydration and depolarization. Proc. Natl. Acad. Sci., vol. 109, pp. 14405–14409.
15. Berg JM, Eriksson LGT, Claesson PM, and Borve KGN (1994) Three-component langmuir-blodgett films with a controllable degree of polarity. Langmuir, vol. 10, no. 4, pp. 1225–1234.
16. Yoon RH and Ravishankar S (1996) Long-range hydrophobic forces between mica surfaces in dodecylammonium chloride solutions in the presence of dodecanol. J. Coll. Int. Sci., vol. 179, no. 2, pp. 391 – 402.
17. Ishida N, Kinoshita N, Miyahara M, and Higashitani K (1999)Effects of hydrophobizing methods of surfaces on the interaction in aqueous solutions. Journal of Colloid and Interface Science, 216, no. 2, pp. 387 – 393.
18. Considine RF and Drummond CJ (2000) Long-range force of attraction between solvophobic surfaces in water and organic liquids containing dissolved air. Langmuir, 16, no. 2, pp. 631–635.
19. Kanduč M, Schneck E, and Netz RR (2014) Attraction between hydrated hydrophilic surfaces. Chem. Phys. Lett., vol. 610, pp. 375 – 380.
20. Nel AR et al. (2009) Understanding biophysicochemical interactions at the nano-bio interface. Nat Mater, vol. 8, pp. 543–557.
21. Jones S and Thornton JM (1996) Principles of protein-protein interactions. Proc Natl Acad Sci, 93, no. 1, pp. 13–20.
22. Yoon RH, Flinn DH, and Rabinovich YI (1997)Hydrophobic interactions between dissimilar surfaces. Journal of Colloid and Interface Science, 185, pp. 363 – 370.
23. Freitas AM and Sharma MM (2001) Detachment of particles from surfaces: An {AFM} study. J. Coll. Int. Sci., vol. 233, no. 1, pp. 73 – 82.
24. Lee JH and Meredith JC (2011) Non-dlvo silica interaction forces in nmpwater mixtures. ii. an asymmetric system. Langmuir, vol. 27, no. 16, pp. 10000–10006.
25. Faghihnejad A and Zeng H (2013) Interaction mechanism between hydrophobic and hydrophilic surfaces: Using polystyrene and mica as a model system. Langmuir, vol. 29, no. 40, pp. 12443–12451.
26. Troncoso P et al. (2014) Nanoscale adhesive forces between silica surfaces in aqueous solutions," J. Coll. Int. Sci., vol. 424, no. 0, pp. 56 – 61.
27. Leung K, Luzar A, and Bratko D (2003) Dynamics of capillary drying in water," Phys. Rev. Lett., vol. 90, p. 065502.
28. Mastropietro DJ and Ducker WA (2012) Forces between hydrophobic solids in concentrated aqueous salt solution. Physical Review Letters, vol. 108, p. 106101.
29. Attard P (2003)Nanobubbles and the hydrophobic attraction. Advances in Colloid and Interface Science, vol. 104, no. 13, pp. 75 – 91.
30. Pertsin A and Grunze M (2012) Computer simulation of adhesion between hydrophilic and hydrophobic self-assembled monolayers in water. J Chem Phys, 137, no. 5, p. 054701.
31. Grzelak EM and Errington JR (2008) Computation of interfacial properties via grand canonical transition matrix monte carlo simulation. J Chem Phys, vol. 128, no. 1, p. 014710.
32. Sedlmeier F and Netz RR (2013) Solvation thermodynamics and heat capacity of polar and charged solutes in water. J Chem Phys, vol. 138, no. 11, p. 115101.
33. Bonn D, Eggers J, Indekeu J, Meunier J, and Rolley E (2009) Wetting and spreading. Rev Mod Phys, vol. 81, pp. 739–805.
34. French RH et al. (2010) Long range interactions in nanoscale science Rev Mod Phys, vol. 82, pp. 1887–1944.